Characterizing Photon Reabsorption in Quantum Dot-Polymer Composites for Use as Displacement Sensors
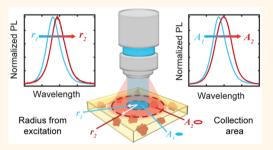
Matthew A. Koc,[†,‡,Δ] Shilpa N. Raja,[‡,§,Δ] Lindsey A. Hanson,[†,‡] Son C. Nguyen,[†,‖]
Nicholas J. Borys,[‡,⊥] Alexander S. Powers,[†] Siva Wu,[¶,□] Kaori Takano,[†,‡,#,■] Joseph K. Swabeck,[†,‡]
Jacob H. Olshansky,[†,‡] Liwei Lin,[∇] Robert O. Ritchie,[‡,§,∇] and A. Paul Alivisatos*[†,‡,§,⊗]

[†]Department of Chemistry, University of California, Berkeley, California 94720, United States
[‡]Materials Sciences Division, Lawrence Berkeley National Laboratory, Berkeley, California 94720, United States
[§]Department of Materials Science and Engineering, University of California, Berkeley, California 94720, United States
[‖]The Hamburg Centre for Ultrafast Imaging, University of Hamburg, Luruper Chaussee 149, 22761 Hamburg, Germany
[⊥]Molecular Foundry, Lawrence Berkeley National Laboratory, Berkeley, California 94720, United States
[¶]Biological Sciences Division, Lawrence Berkeley National Laboratory, Berkeley, California 94720, United States
[#]JX Nippon Oil & Energy Corporation, 8, Chidori-cho, Naka-ku, Yokohama-shi, Kanagawa 231-0815, Japan
[∇]Department of Mechanical Engineering, University of California, Berkeley, California 94720, United States
[⊗]Kavli Energy NanoScience Institute, Berkeley, California 94720, United States

Ⓢ Supporting Information

ABSTRACT: The reabsorption of photoluminescence within a medium, an effect known as the inner filter effect (IFE), has been well studied in solutions, but has garnered less attention in regards to solid-state nanocomposites. Photoluminescence from a quantum dot (QD) can selectively excite larger QDs around it resulting in a net red-shift in the reemitted photon. In CdSe/CdS core/shell QD-polymer nanocomposites, we observe a large spectral red-shift of over a third of the line width of the photoluminescence of the nanocomposites over a distance of 100 μm resulting from the IFE. Unlike fluorescent dyes, which do not show a large IFE red-shift, QDs have a component of inhomogeneous broadening that originates from their size distribution and quantum confinement. By controlling the photoluminescence broadening as well as the sample dispersion and concentration, we show that the magnitude of the IFE within the nanocomposite can be tuned. We further demonstrate that this shift can be exploited in order to spectroscopically monitor the vertical displacement of a nanocomposite in a fluorescence microscope. Large energetic shifts in the measured emission with displacement can be maximized, resulting in a displacement sensor with submicrometer resolution. We further show that the composite can be easily attached to biological samples and is able to measure deformations with high temporal and spatial precision.

KEYWORDS: quantum dots, inner filter effect, nanocomposite, photon recycling, sensor, photoluminescence, fluorescence

Fluorescence spectroscopy is widely used in biochemistry and analytical chemistry because of its high sensitivity. One potential issue in using fluorescence as a quantitative tool, however, is that the intensity of the fluorescence is not simply proportional to the concentration of fluorophore, due to the inner filter effect (IFE).[1,2] The IFE is the self-quenching of a fluorophore by the absorption of a sample's photoluminescence (PL). At high concentrations of fluorophores, the measured PL quantum yield (PLQY) is lower than the true PLQY of the fluorophore, owing to the increased self-absorption. At its extreme, the IFE can result in a significant

spectral change based upon the overlap of the absorption and PL of the fluorophore.[3-7] Because of the nonlinearity and major spectral changes that can occur from the IFE, it is typically viewed as a hindrance in most experiments.[1-7] In solutions, the simplest method to eliminate the IFE from measurements is to decrease the sample concentration, decreasing the optical density at the emission wavelength.

Because of this, most PL properties are typically only investigated for dilute samples.

Despite most researchers designing experiments to carefully avoid the IFE, it has seen a few potential uses in the detection of ions or small molecules in solution.[3−6] Typically, these sensors are composed of a binary mixture of an absorber whose absorption changes upon the binding of an analyte and a fluorophore whose PL is independent of the analyte. With careful tuning of the PL and absorption overlap, large changes in PL properties of the mixture can be observed upon the addition of small concentrations of analyte.

The use of fluorophores in solid-state applications generally differs greatly from solution-based applications. Many solid-state applications require fluorophores to be concentrated into films or polymers in order to enhance the PL intensity of the device. Devices such as light emitting diodes,[8−11] luminescent solar concentrators,[12,13] wide color gamut backlit displays,[14−16] and stress-sensing quantum dot (QD)-polymer composites,[17,18] generally operate more efficiently at higher concentrations of the fluorophore, but this makes them more prone to self-quenching and spectral changes. The IFE has not been well characterized in solid-state systems and it is unclear as to how detrimental the IFE could be for devices that depend upon light emission. Further, to the best of our knowledge, the use of inner filtering for sensing using QD arrays or clusters, in the solid-state or in structural polymers has never been demonstrated.

Here we demonstrate a thorough characterization of the IFE in QD-polymer composites using an array of techniques including transmission electron microscopy (TEM), wide-field and confocal-fluorescence microscopy, and time-resolved emission spectroscopy (TRES). Despite the high degree of monodispersity of our QDs, an appreciable shift in the PL emission due to the IFE is still observable. By careful investigation of the relation of the PL properties to the nanostructure of the composites, we propose how one could either increase or decrease the amount of the IFE occurring in the solid state. We further show how these nanocomposites can exploit the IFE and can be used as an entirely spectroscopic z-height sensor that is capable of measuring submicrometer z-deflections in both mechanical and biological systems. The nanocomposites in this work can be used to sense static and oscillatory vertical deformation with high spatiotemporal resolution and can easily interface with tissues to monitor biological deformation. Unlike existing techniques for measuring biomechanics,[19,20] our nanocomposites could provide autofocus monitoring on a flexible substrate with submicrometer resolution. This technique could also be useful in applications such as monitoring the pressure of membranes used for gas penetration.[21]

RESULTS AND DISCUSSION

Characterization of the IFE in QD-Polymer Nanocomposites. Monodisperse CdSe/CdS core/shell QDs of diameter 7.0 ± 0.5 nm, with a PL emission maximum of 615 nm with a full width at half-maximum (fwhm) of 22 nm, were prepared *via* standard colloidal synthetic techniques.[22,23] The QDs were mixed with a solution of poly(styrene-ethylene-butylene-styrene) (SEBS) in chloroform and were cast into Petri dishes and dried overnight, forming ~100 μm thick films of QD-SEBS nanocomposites.[18,24] Because there is not a favorable enthalpic interaction between the QD ligand shell and the polymer, the QDs tend to aggregate upon evaporation of

the chloroform[18,24] as seen in the TEM image of a microtomed sample in Figure 1. Due to the slow drying process, the QDs are observed to aggregate into clusters, as shown in Figure 1b.
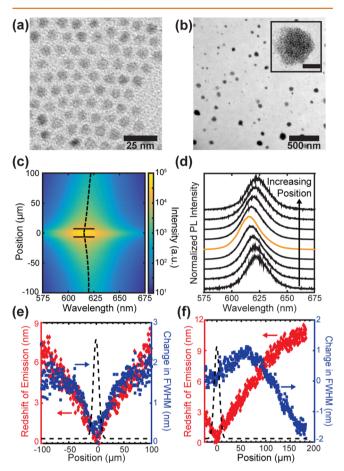

Figure 1. TEM of (a) as-synthesized CdSe/CdS core/shell QDs and (b) microtomed sample of 5% QD-SEBS nanocomposite. Inset shows an example cluster with a scale bar of 100 nm. (c) A PL spectral map of a QD-polymer composite excited at 488 nm. Position is a measure of the distance from center of excitation. Black lines show the beam diameter and the dotted line is a guide for the emission maximum at each position. (d) Normalized PL measured every 25 μm from (c). The orange spectrum indicates the emission at the center of the excitation. (e,f) Measured red-shift (red) and change in fwhm (blue) of the emission as a function of distance from excitation center for two different excitation locations on the film. The black line represents the normalized excitation intensity.

The PL of the nanocomposites was investigated using a home-built, inverted fluorescence microscope setup with a 488 nm laser excitation source, which was used to locally excite the sample. The diameter of the excitation area was varied from ~1 to 150 μm at the beam waist at a power density of ~0.2 W/cm². Using a spectrometer and imaging CCD, spatially resolved emission spectra were recorded along one spatial direction as shown in Figure 1c, where the 0 μm position corresponds to the center of the laser excitation spot. The emission intensity is plotted on a log-scale to more easily show the spectral peak shifting as a function of distance from the center of excitation. The two horizontal lines represent the beam diameter $(1/e^2)$ and the dotted line is included to as a guide to the eye for the emission maximum at each position.

The PL of the dots excited by the laser, hereby "primary excitation", was measured to have an emission maximum around 617 nm. This is slightly red-shifted from dilute solution PL measurements and can be attributed to a change in the dielectric constant of the surrounding environment of the dots and Förster Resonance Energy Transfer (FRET) within an aggregate.[25] Fluorescence was observed far (>100 μm) from the central position of primary excitation, indicating that the QDs are being excited by a secondary source from within the sample. The PL emission maximum monotonically red-shifts with increasing distance from the center of primary excitation, r. Normalized, stacked spectra from Figure 1c are shown in Figure 1d to more clearly illustrate the emission maximum red-shift. We also explicitly show how the emission maximum (red) and fwhm (blue) of the sample change with increasing distance from the center of the primary excitation region in Figures 1e and f. The dotted black line indicates the location and intensity of the primary excitation incident upon the sample.

The continuous shift of PL to lower energies with increasing distance from the region of primary excitation manifests from the IFE within the solid-state composite. The nanocomposite is initially excited locally in the region of the primary excitation. The emission from QDs within this region is isotropic and can either exit the sample or be reabsorbed by a quantum dot with a lower-energy bandgap, which can then subsequently undergo radiative relaxation and emit a lower-energy photon. This process of reabsorption and emission naturally favors a reduction in the energy of the recycled photon because even though the QDs have a broad absorption spectrum, emission is most efficient at the lowest-energy excited state. Further, due to the intrinsic Stokes shifts of QDs, only larger QDs with smaller band gaps can reabsorb these secondary photons.[26,27] At distances further than the primary excitation area, collected photons are more likely to have undergone one or more recycling steps because of the longer path traveled through the sample and are thus at lower average energies than the PL from the region of primary excitation.

The initial broadening of the PL with increasing position from the region of primary excitation is a bit puzzling. The nature of the IFE should progressively excite smaller ensembles of larger particles leading to an overall reduction in the inhomogeneous broadening and ultimate narrowing of the PL. However, within the first 50 μm, the fwhm of the emission shows a subtle increase. We attribute this initial increase to the convolution of emission from the region of primary excitation with that of secondary emission from recycled photons. Such a convolution would decrease with increasing distance but overall broaden the PL to lower energies. The primary excitation excites all QDs within the region and the primary PL intensity at a given wavelength is dependent only upon the size distribution. The secondary excitation excites a subset of this population, whose PL intensity now depends upon the population of secondary excited dots and the primary PL intensity. The secondary excitation will produce PL that is red-shifted from the primary photon, due to the Stokes shift in the QDs.[26,27] Thus, we have contributions from two groups of emitters whose emission centers are approximately separated by the Stokes shift. The measured PL near primary excitation is a combination of the primary emission and the secondary emission and would be expected to broaden while the emission from primary and secondary emitters are of similar intensities. The eventual narrowing is due to the decreased intensity of the primary emission and is indicative of selectively exciting a single

population of QDs.[28] As distance from the primary excitation increases, the relative intensity of emission from the largest dots increases, as those are the only dots being excited. At nearly 200 μm from excitation, the fwhm is less than 20 nm (~65 meV). This narrow line width approaches the room temperature fwhm measured for single cadmium chalcogenide QDs and is in agreement with homogeneous broadening by phonon dephasing (50–60 meV).[29–31] It is expected that at a distance far from excitation, the only emission we would observe would be that from the single largest dot in the sample.

Further evidence of the IFE was observed by investigating the importance of photon transport within the films. Nanocomposite films (index of refraction ~1.5) were placed in contact with media of varying indices of refraction (1 to ~1.5). By increasing the refractive index of the medium surrounding the nanocomposite, we decreased the number of photons traveling within the composite by decreasing the degree of total internal reflection. Films immersed in water and immersion oil showed a 60–75% decrease in red-shift relative to films suspended in air. This, in conjunction with its radial symmetry (Figures 1c,e), indicates the importance of intrasample photon transportation to the observed shifts, all of which are consistent with IFE being the mechanism underlying the red-shift.

With regards to the origin of the spectral shift, we have considered and eliminated other mechanisms, such as FRET, spatial inhomogeneity of the nanocomposite, and laser-induced heating. TRES decay transients of the nanocomposite at longer wavelengths show longer lifetimes than at shorter wavelengths (Figure 2a). In combination with the slow rise time at longer wavelengths, there are clear FRET signatures within the polymer-nanocomposite.[32] Despite these clear FRET signatures, FRET cannot be responsible for the large red-shift over the large length scale observed in Figure 1. Specifically, FRET
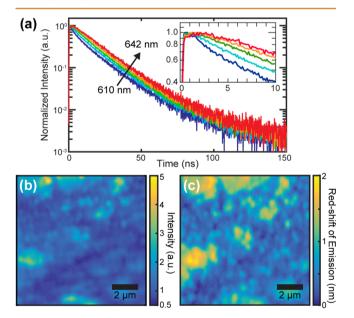

Figure 2. (a) TRES decays for a 5% loading by mass QD-SEBS nanocomposite. As emission wavelength increases, the lifetime is shown to increase as well as have a rise time as shown in the inset. (b,c) Confocal PL spectral map of a 1.25% QD-SEBS nanocomposite excited with 488 nm cw-laser and plotted with a pixel size of 100 × 100 nm². A correlation between (b) integrated peak intensity and (c) red-shift of the PL from the bluest measured spectrum.
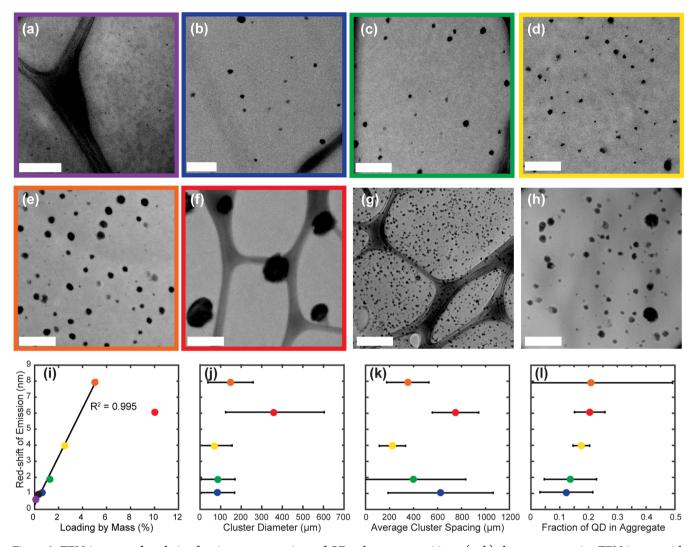
Figure 3. TEM images and analysis of various concentrations of QD-polymer compositions. (a−h) show representative TEM images with scale bars of 200 nm (a) and 500 nm (b−h). QD-SEBS composites at 0.05% (a), 0.625% (b), 1.25% (c), 2.5% (d), 5.0% (e), and 10.0% (f). QD-PLLA at 5% (g) and QD-PCL at 5% (h) are also shown. Large linear features are from the lacey carbon support. (i−l) Image analysis of the QD-SEBS samples relating the red-shift of emission to the mass loading (i), cluster diameter (j), cluster spacing (k), and fraction of QD in aggregate (l). Data points are color coded to show same sample between different plots. All plots show standard errors from image analysis and peak fitting.

efficiency falls off with a $1/R^6$ distance-dependence and is thus an *intra*-cluster effect that is limited to the spatial extents of the clustering of the quantum dots in the nanocomposites.[32] The effect reported in Figure 1 is an *inter*-cluster effect that operates on a much longer length scale, such that the energy transfer between clusters cannot be explained by FRET. This was further verified by investigating the extent to which FRET changes the PL spectra in our system. The PL of an aggregate with strong FRET interactions will exhibit a red-shifted PL compared to an ensemble of isolated QDs, such as that in a dilute solution or solid-state dispersion. From TEM characterization, we know that our composites have both regions of dispersed QDs and clustered QDs, so we used micro-photoluminescence to assess the spatial variations of the PL within our sample (Figures 2b,c). In contrast to the measurements in Figure 1, the micro-PL measurements only collect emission from the region of primary excitation. In this excitation and collection scheme, we find that the areas that exhibit the greatest red-shift are highly correlated to the highest intensity, indicating that more QDs are being excited. At most,

however, when the excitation and collection volumes are the same, we only observe a 2 nm red-shift over a large sample area, which is far smaller than the shifts observed in the wide-field configuration presented in Figure 1, further indicating that FRET is insufficient to explain the shifts observed.

To rule out any laser-induced effects, the primary excitation power density was varied over 4 orders of magnitude from ~10^{-2} to ~10^2 W/cm^2; while simultaneously measuring the PL, the temperature of the sample was monitored with a thermal camera (FLIR corporation) with ~4 μm spatial resolution. We did not observe any detectable temperature rise or laser-induced red-shifts by varying the excitation power density near the flux regimes used in this work (Figure S1a). Further, it is known that the angle of total internal reflection is wavelength-dependent; however, changing the collection angle of the detector over 40° from normal showed less than a 1 nm red-shift. Thus, we may conclude that any shifts due to changing collection angle are insufficient to describe the observed effect (Figure S1b). Through all of these controls, we further

conclude that the red-shift originates predominately from the IFE.

Tuning the IFE-Induced Red-Shift. The concentration dependence of the IFE is more complex in the solid state than in solution as we can no longer assume that the sample is homogeneous.[1,2] Clear evidence of aggregation of QDs is observed in the TEM and micro-PL scans, so we also have to consider how changes in cluster size, density, and spacing can affect the overall shift observed. Precise control of QD dispersion in polymers still remains a synthetic challenge,[18,33] which makes it difficult fully explore these variables. By modifying the QD-polymer interactions we are able to change the QD dispersion and offer correlations that we observed in our samples and possible explanations for these correlations.

The IFE emission red-shift at 100 μm from the center of primary excitation ($\sim$5 μm beam diameter) was measured for QD-SEBS, QD-poly(L-lactic acid) (PLLA), and QD-polycap-rolactone (PCL) nanocomposites with concentrations varying from 0.05% to 10% by mass (Figure 3, Table S1, S2). QD-PLLA samples were observed to be more dispersed than either QD-SEBS or QD-PCL samples at the same concentration, likely due to the miscibility of ligands in PLLA. Composites in which QDs were singly dispersed (i.e., had no cluster formation) did not exhibit measurable red-shifts. The red-shift was generally strongest in the most optically dense composites, consistent with the mechanism of the IFE;[1,2,6] however, we found that at our highest loading of 10% by mass in the QD-SEBS nanocomposite, the sample had a decreased shift compared to the 5% loading in the same system (Figure 3i). Although there was an increase in QD concentration, the average size, spacing, and density of clusters changed as well. These changes in the dispersion of the QDs can have large effects on the number of reabsorption events a photon undergoes. For the range of concentrations investigated, neither the average cluster diameter, nor the average cluster spacing, show a clear correlation with the IFE induced red-shift; only the fraction of QDs in the aggregate, a proxy for cluster density, shows a purely monotonic trend with the red-shift (Figure 3j–l).

One possible explanation is that the IFE shift is also dependent upon the photon scattering within the sample. The index of refraction in a composite can be approximated as the linearly weighted average of the volume fractions, thus higher density clusters (i.e., clusters with a greater QD volume fraction) will have a higher index of refraction than a lower density cluster, increasing the scattering cross-section at that interface.[34] In a completely nonscattering composite, an emitted photon will simply travel through the composite away from the point of emission until it is reabsorbed. For a thin, nonscattering sample, we could approximate the path length that the photon traversed as simply the radial-distance from emission. In the case of a photon being emitted in a scattering composite, the photon can scatter back toward the QD that it was emitted from before being absorbed.[34] Thus, for a photon in a scattering medium to reach the same radial-distance from initial emission, it will have to travel a longer path on average than a photon in a nonscattering medium. Such an increase in the photon's path length will increase the likelihood of reabsorption events from the IFE and cause a greater red-shift in the sample.[1,2]

Another possible explanation is that the aggregated samples show a greater red-shift because photon reabsorption in a cluster can also result in additional FRET events within that cluster before it is reemitted. In this case, the energy is red-shifted from both the IFE and FRET, but IFE can transport the energy from one cluster to another across the nanocomposite allowing for the large distance of energy transfer that is observed in our systems. Consequently, for an aggregated sample, a single photon absorption/reemission event could consist of more than one energy transfer event, whereas a well-dispersed sample would only have a single energy transfer event per photon absorption/reemission event.

We further investigated how the shape of the CdSe/CdS heterostructure incorporated in the nanocomposite could affect the observed IFE shift. At the same loading by core mass, the spherical QDs exhibited the greatest shift, followed by nanorods, and finally nanotetrapods, which had little to no shifts (Figure S2, Table S2). From TEM, the tetrapods are observed to inefficiently pack and generate the least dense aggregates, while the spherical dots are observed to have the densest aggregates. This observation further supports the claim that scattering increases the IFE in solid samples, but we refer the reader to the Supporting Information for a more thorough description of the QD shape dependence. Among the various tested samples, we found the sample at 5 wt % of CdSe/CdS spherical QD in SEBS showed the greatest IFE red-shift.

Unlike QDs, laser dyes (rhodamine 640 and rhodamine 575) that were dispersed in the same polymer and had little to no observable red-shift. Although these samples certainly undergo the process of inner filtering, changes in PL peak maximum are more difficult to measure due to the broad line width (fwhm $\sim$150 nm) and the small overlap of absorption and PL which results in a low efficiency of the IFE red-shift for each recycled photon.[35] The inhomogeneity of absorption inherent in a nonuniform population can actually result in a greater red-shift than an ensemble of organic molecules whose absorption is homogeneous. In inhomogeneous populations, FRET and reabsorption events favor the transfer of energy to subpopulations with excited state energies that are lower than the donor state. As such, QDs appear to be particularly suited to IFE-induced red-shifts due to their strong absorption, size dispersion, and quantum confinement.

Using the IFE as a Displacement Sensor. We sought to explore the potential of using the IFE in our composites to serve as a height sensor. By locally exciting a small area of the nanocomposite with a fluorescence microscope we can create a material whose luminescence red-shifts monotonically about the center of the excitation from the IFE (Figure 1). This radially symmetric shift provides a system with the unusual property that the measured emission maximum at the center of excitation shifts in a predictable manner by simply changing the objective to sample distance, z. A reversible red-shift in PL is observed upon under- and overfocusing of the microscope as shown in Figure 4a. It is important to note that this sort of a red-shift does not originate exclusively from the IFE, like was the case in Figure 1. Rather, it originates from the emission symmetry and the optical path through which the emission is collected.

A schematic representation of the fluorescence microscope setup is shown in Figure 4b. When focused, that is when $z = f_O$, the focal length of the objective, light from a single point in the sample can be mapped onto a single point on the detector, or conversely, a single point on the detector can be mapped onto a single point on the sample. As z is moved by some displacement Δ, a single point on the detector now is mapped
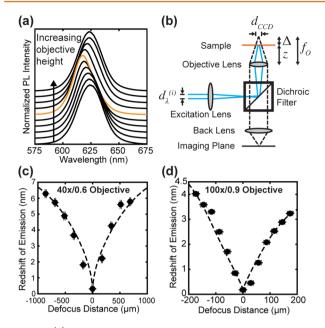
Figure 4. (a) Stacked PL spectra of composites as a function of z. Moving z from focus (orange spectrum) in either direction causes a red-shift in the PL spectrum. (b) Schematic of inverted fluorescence microscope. The composite is excited and PL is collected through the same objective and directed to a spectrometer. (c,d) The measured (circles) and modeled (dashed) red-shift in collected PL upon a change in height or focus for a (c) 40× (0.6 NA) and (d) 100× (0.9 NA) objectives. Error bars are the standard errors.

onto a spot of diameter d_{CCD}. Assuming that the objective can be modeled as a simple lens, we can see that

$$ d_{CCD} = \frac{d_O}{f_O}|\Delta| \tag{1} $$

where d_O and f_O are the objective lens diameter and focal length, respectively, and the magnitude of d_{CCD} is dependent upon the defocus distance, Δ.

The measured spectrum, Φ_{meas}, will be a sum of all the emitted light in a circle of diameter d_{CCD}, weighted by the intensity of the emission source.[36] We can model the detected spectrum as an intensity-weighted sum of a radially independent spectrum, $\Phi_P(\lambda)$, attributed to the primary emission, and a radially dependent spectrum, $\Phi_{IF}(\lambda,r)$,

attributed to the secondary emission of the IFE, where r is the radial distance from the center of primary excitation. Thus, the measured spectrum as a function of defocus distance is given by

$$ \Phi_{meas}(\lambda, \Delta) \propto \int_0^{d_{CCD}/2} (I_P(d_\lambda^{(f)}(\Delta), r)\Phi_P(\lambda) + I_{IF}(r)\Phi_{IF}(\lambda, r))r \, dr \tag{2} $$

where the intensities of the primary emission and secondary emission are I_P and I_{IF}, respectively. The PL spectrum from secondary emission, Φ_{IF}, is modeled using the spatial dependence of the shift measured in Figure 1E, but is assumed to be independent of the defocus distance (Figure S3). The primary intensity, I_P, depends upon the distance from focus, Δ, and the distance from the center of excitation, r. In focus, I_P has a Gaussian profile and is assumed to broaden[36] to a width of $d_\lambda^{(f)}$ as the distance from focus is changed. The increased spot size can be estimated with geometric optics based on the incoming beam diameter, $d_\lambda^{(i)}$, the focal length of the excitation lens, f_λ, and the path length between the excitation lens and objective lens, h

$$ d_\lambda^{(f)}(\Delta) = \frac{d_\lambda^{(i)}}{f_O f_\lambda}(\Delta^2 + \Delta(h - f_O) + f_O^2) \tag{3} $$

This empirical model fits well to the experimentally measured red-shifts as shown in Figure 4 where the microscope objective was changed from a 40×, 0.6 Numerical Aperture (NA) objective (Figure 4c) to a 100×, 0.9 NA objective (Figure 4d). The asymmetry in the shift, particularly present with the 100× objective, is well captured in the model. This asymmetry comes from the asymmetric change in the laser spot size upon changing the focus of the sample. By removing the back lens, the model predicts that the shift will be symmetric with increasing and decreasing focus.

Near the focus of the sample, the red-shift in emission maximum can be approximated as linear with a red-shift of 0.01 and 0.02 nm/μm for the 40× and 100× objectives, respectively. The statistical error in our peak fitting was measured to be 2.3 × 10^{-3} nm (Figure S4), indicating that it is possible to detect displacements with submicrometer precision, specifically with ~460 nm and ~230 nm z-resolution for the 40× and 100× objectives, respectively.
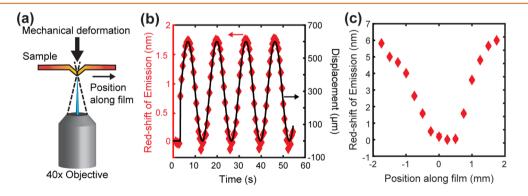

Figure 5. (a) A schematic of sample positioning relative to the objective for measuring deformations. (b) The measured PL shift (red) of the sample for a given deformation (black) of sample by a piezoelectric driver shows good, repeatable tracking of mechanical oscillations. (c) 1D spatial map of red-shift of the sample under static deformation with a blunt indentation probe. Error bars are standard errors peak fitting, but are small enough to be hidden within the data points.

We note that improved resolution can be achieved either through optical path engineering (eqs 1 and 3) or through nanocomposite engineering (changing Φ_P and Φ_{IF}). For example, the optical path can by optimized by changing the objective collecting the emission. When we changed from the 40× to the 100× objective we increased the rate of convolution and observed a factor of 2 increase in the resolution. By using samples with a greater IFE red-shift we imagine we could further improve this resolution. It is worth noting that our model implies that this shift can be achieved solely from the optics used and should be true for any emitter with a radially symmetric monotonic shift, not just one created by the IFE.

Because this red-shift monotonically increases with defocus, the location of the emission maximum could be used as a vertical deformation sensor. To determine the ability of the nanocomposite to sense deformations, we tested the temporal response of our system with respect to a small-point deformation of the sample (Figure 5a). A piezoelectric motor was used to depress the composite up to 600 μm in a sinusoidal motion. The fluorescence of the sample and the film position were simultaneously measured and are shown in Figure 5b. There is good agreement between the measured red-shift of the emission (red diamonds) and the physical displacement (black line). The IFE-induced red-shift is fully reversible with no hysteresis and tracks the mechanical deformation with a high degree of precision. Because this process is purely spectroscopic, the temporal resolution is only limited by the submicrosecond photon transport within the film,[26] and by our detector's temporal resolution of, in this case, ~0.1 s; it could be much higher with other commercially available rapid imaging detectors, such as electron multiplied CCDs (EMCCDs) or scientific CMOS detectors.

By manually scanning the sample, we show that this technique can be used to map out the spatial profile of an applied deformation. Upon indentation with a ~500 μm diameter probe into the nanocomposite, we scanned the sample across the wide-field optical excitation area (~150 μm diameter spot), recording the PL emission at each position in 250 μm steps (Figure 5c). Using the known mechanical properties of membranes under z-deflections, it should be straightforward to analytically convert observed strains or deformations to stresses.[37] Such a technique could be useful in measuring the stresses and strains within various polymer membranes noninvasively. As this is a visible light fluorescence-based technique, we expect that this technique should be able to achieve submicrometer lateral resolution in addition to the submicrometer vertical resolution.

The performance of the QD-polymer composite as a height sensor also shows promise for a variety of biological processes. Because this shift is seen in multiple polymers with multiple types of nanocrystals, this type of composite should allow researchers to create a biocompatible substrate for investigating biological deformations. As a proof of concept, we show that a nanocomposite can adhere to the surface of a lung and easily detect the movement associated with the inflation and deflation of the lung (Figure 6). A nanocomposite film was placed on the surface of a chicken lung to which it readily adhered without any adhesives. The lung was mounted on an inverted fluorescence microscope (Figure S5) and respiration was simulated via a nitrogen inlet attached to the trachea. The PL of the sample was measured as the lung was sequentially inflated and deflated (Figure 6b). When inflated, we detected a vertical displacement of the bottom of the lung of around 250
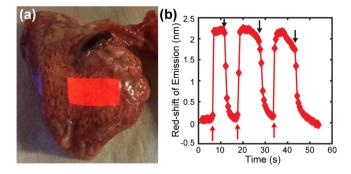

Figure 6. Monitoring deformation of an artificially respired chicken lung. (a) Photograph of a nanocomposite adhered to surface of a chicken lung via van der Waals forces under UV illumination. (b) PL red-shift as a function of time and respiration. The red arrows indicate inflation and the black arrows indicate deflation. Error bars are standard errors from peak fitting, but are small enough to be hidden within the data points.

μm and upon deflation, a clear relaxation back to the baseline was observed. Similar deformations were observed by Nguyen et al.[38] with a piezoelectric sensor on an artificially respired lung.

Although those sorts of large-scale deformations can also be studied by other techniques,[20,39] this nanocomposite may have the potential to be applied to looking at intercellular deformations.[19,40−42] Frequently, stiff substrates are used to support cell cultures and other biological specimens examined in fluorescence microscopes. These inhibit the full range of transverse motion of biological specimens and severely limit the ability to study important biological processes such as wound healing and cancer cell proliferation that depend on the mechanical environment. Because of the use of a stiff substrate, vertical deformations in these processes have received less attention and are less well-determined than biological deformations in the lateral, $x-y$ plane.[43−45] With a soft composite, such as QD-polymer, this technique may be able to image the dynamics of live cells, which is not yet easily measurable noninvasively.[19,46]

CONCLUSIONS

Our work has demonstrated the importance of understanding how the IFE can affect the PL properties of QD-polymer composites. The size dispersity inherent in colloidal nanoparticle synthesis provides enough heterogeneity that the PL red-shifts over a third of the initial peak width within 100 μm of spatial distance within these composites. This emphasizes the need for increased synthetic control of monodispersity in QD synthesis, particularly for applications where spectral purity is important. Further, control of the dispersion of QDs in polymers is an important parameter to control the extent by which the IFE is occurring in the solid-state. Well-dispersed composites show a substantial decrease in the IFE-induced red-shift compared to highly aggregated samples.

We also demonstrated that the red-shift caused by the IFE can be used as a quantitative real-time optical height sensor with submicrometer resolution in the z-dimension. Further developments could result in greater shifts by using thinner and longer polymer nanocomposite geometries,[37] softer polymers, or by increasing the scattering properties of the sample. Future applications could be diverse, including pressure-sensing membranes, metrology-sensing adhesives and coatings, and sensing z-stresses involved in tissue growth[43] and cell

locomotion,[47] as well as a variety of other small-scale biological processes that have been challenging to noninvasively study in a low-cost format with high spatiotemporal resolution.

METHODS

Materials. Trioctylphosphine oxide (TOPO, 99%), selenium (Se, 99.99%), cadmium oxide (CdO, ≥99.99%), oleic acid (OA, 90%), 1-octadecene (ODE, 90%), oleylamine (OLAM, 70%), and 1-octanethiol (OctSH, ≥98.5%) were purchased from Sigma-Aldrich. Tri-*n*-octylphosphine (TOP, 99%) was purchased from STREM, octadecyl-phosphonic acid (ODPA, 99%) from PCI Synthesis, and sulfur (S, 99.9995%) from Alfa Aesar. All chemicals were used in the as-received condition. Laser dyes rhodamine 640 and rhodamine 575 were purchased from Exciton. Poly(styrene-ethylene-butylene-styrene) (SEBS, MD-1537, molecular weight of 117 kDa) was provided by Kraton Corporation. Polycaprolactone (PCL, molecular weight of 80 kDa) was purchased from Sigma-Aldrich, and poly l-lactide (PLLA, molecular weight of 100 kDa) was purchased from ShenZhen ESUN Industrial Co. Ltd. Other chemicals used include the anhydrous solvents acetone, chloroform, toluene, methyl acetate, and hexanes.

CdSe Core Synthesis. Wurtzite CdSe cores (w-CdSe) were synthesized following a previously reported procedure.[23] In a typical reaction, 3 g of TOPO, 280 mg of ODPA, and 60 mg of CdO were combined in a 25 mL round-bottomed flask, and degassed under vacuum at 150 °C for 30 min. The reaction vessel was then heated to 320 °C under flowing argon until complete complexation of Cd was achieved. To the reaction, 1 mL of TOP was injected into the reaction solution, which was then heated to 375 °C for the fast injection of Se (60 mg) dissolved in TOP (0.5 mL). Upon injection, CdSe nanocrystals were allowed to grow for 10−30 s and the reaction was cooled to room temperature. QDs were cleaned in an inert atmosphere with successive precipitation and dissolution using toluene/acetone, CHCl$_3$/IPA, and hexanes/acetone as solvent/antisolvent pairs, and were redispersed in hexanes. Overnight, a gel fraction gradually formed, presumably unreacted precursors, and was removed by centrifugation and the supernatant was filtered with a 0.2 μm pore PTFE syringe filter.[48] The cores were stored in hexanes in an inert environment. Sizing and concentrations were determined by a previously reported empirical formula.[49]

CdSe/CdS Core/Shell Synthesis. CdSe/CdS core/shell QDs were synthesized following previously reported procedures.[50] In a typical reaction, w-CdSe QDs (100−800 nmol) were initially degassed under vacuum at room temperature for 1 h and then at 120 °C for 30 min in a solution with either a 1:1 ratio of OLAM:ODE or a solution of just ODE. The total volume of OLAM and ODE ranged from 3 to 6 mL per 100 nmol of QDs used. The reaction was then heated under argon to 310 °C, and held there for the duration of the shell growth. During the heating, a slow injection of 0.2 M OctSH in ODE and 0.2 M Cd-oleate in ODE was started at 250 °C. Injection solution volumes varied between 6 and 12 mL for each precursor, but the total reaction time of 2 h was maintained. Upon injection completion, the reaction was maintained at 310 °C for 10 min, then cooled to room temperature. The core/shell QDs were isolated from excess ligand *via* precipitation in acetone and redispersion in hexanes, repeated two or three times. Insoluble impurities were removed from solution *via* centrifugation in hexanes without any antisolvent. QDs were stored in either hexanes or chloroform in an inert environment.

QD-Polymer and Laser Dye−Polymer Composite Preparation. QD-polymer composites were prepared similarly to previously reported procedures.[51] In brief, solutions of 1.2% by weight polymer (SEBS, PLLA, and PCL) were mixed with the appropriate concentration of QDs in chloroform to achieve a concentrations ranging from 0.05% to 10% of QD by mass in polymer. Typically, solutions were made with ~140 mg SEBS and ~8 mL chloroform. The QD-polymer solutions were cast into a small glass Petri dish and solvent was allowed to evaporate slowly the course of 8 h, or were dried into a 20 or 7 mL glass vial using an in-house nitrogen line. Resulting films were typically 70−150 μm in thickness. For laser dye−polymer composites, rhodamine 575 or 640 solutions in chloroform

were mixed at very low concentrations (<0.001% by weight) with polymer solutions in chloroform in order to avoid any aggregation-induced shifts.[52] The dye−polymer solutions were cast into glass Petri dishes and dried overnight in ambient conditions.

Inverted Fluorescence Microscope System with Spectrograph. All fluorescence spectra taken in this study were measured on a home-built fluorescence microscope setup, unless otherwise stated. Samples were mounted on an inverted microscope (Zeiss). Samples were excited from below with an Ar$^+$, cw-laser emitting at 488 nm. The typical power density on the sample was ~0.2 W/cm^2. Fluorescence was collected through the same objective used to excite and the laser was scattered off with a dichroic mirror and filter. Photoluminescence was directed to a liquid nitrogen cooled Princeton Instruments Si CCD and was spectrally resolved with a Princeton Instruments Acton 2300 monochromator with a 300 gr/mm grating, blazed at 750 nm. The detector was calibrated daily to ensure spectral accuracy within 0.1 nm.

Transmission Electron Microscopy (TEM) Sample Preparation and Imaging. For TEM, ~70−90 nm sections of PCL, PLLA and SEBS-QD nanocomposites were cut from as-prepared nanocomposite films using an RMC MT-X Ultramicrotome (Boeckler). Sections were cut at cryogenic temperatures and picked up onto copper grids from water. TEM images were acquired using a 200 kV Tecnai G2. For nanoparticle size distributions, more than 200 particles were counted per measurement using Image-J to analyze TEM images.

Time-Resolved Emission Spectroscopy (TRES) Measurements. Time-resolved photoluminescence measurements were performed with a Picoquant FluoTime 300 with a PMA 175 detector. The excitation source was a 407.7 nm LDH−P-C-405 diode laser. Photoluminescence decays were acquired every 2 nm between 550 and 750 nm with a repetition rate of 4.2 MHz and bin width of 128 ps.

Confocal Microscopy. Confocal photoluminescence microscopy was performed with a Zeiss 100×/1.25 NA oil immersion objective on a WITec alpha300R+ upright microscope with 488 nm laser excitation. Emitted light was collected through a 50 μm multimode optical fiber to a UHTS 300 imaging spectrometer with a 600 gr/mm grating blazed at 500 nm. The spectrum was then detected on a thermoelectrically cooled Andor DU970N−BV-353 silicon CCD. Photoluminescence spectra were collected from a 10 μm × 10 μm area of the 1.25% QD-SEBS nanocomposite. The pixel size was 100 nm × 100 nm, and the pixel integration time was 0.1 s.

Temperature Measurements of Photoexcited Nanocomposites. The PL spectra and sample temperature were simultaneously measured with excitation power density ranging from ~10^{-2} to over 10^2 W/cm^2 in order to ensure that the sample was not shifting due to any laser-induced effect, such as heating. Temperatures were measured with a thermal camera (FLIR corporation, Model#: A8303sc with a 4× microscope MWIR SC8X00 objective). Power density at the sample was measured with a power detector purchased from Thor Laboratories. The nanocomposite sample was mounted such that it was in focus of both the FLIR thermal camera and fluorescence microscope objective. Figure S1 shows the fluorescence and measured temperature of the polymer as a function of excitation power density. Aside from these measurements, all experiments in this report were performed with excitation power densities of less than 1 W/cm^2; thus, we do not see any heat induced effects.[53] We also see that the emission does not change over this range of fluxes.

ASSOCIATED CONTENT

Ⓢ Supporting Information

The Supporting Information is available free of charge on the ACS Publications website at DOI: 10.1021/acsnano.6b08277.

> Synthesis and TEM images of nanorod and tetrapod CdSe/CdS nanocomposites; IFE control experiments; biological sensing setup; supplementary discussion of TEM image analysis and errors associated with peak fitting; Tables S1−S3 (PDF)

AUTHOR INFORMATION

Corresponding Author

*E-mail: paul.alivisatos@berkeley.edu.

ORCID

Matthew A. Koc: 0000-0003-1401-8415
Shilpa N. Raja: 0000-0001-5641-8930
Nicholas J. Borys: 0000-0001-5434-1191
Jacob H. Olshansky: 0000-0003-3658-1487
Robert O. Ritchie: 0000-0002-2501-6998
A. Paul Alivisatos: 0000-0001-6895-9048

Present Addresses

■School of Materials and Chemical Technology, Tokyo Institute of Technology, 4259 Nagatsuta-cho, Midori-ku, Yokohama-shi, Kanagawa, 226−8503, Japan.
□Viral Forensics, LLC, Berkeley, California, 94710, United States.

Author Contributions

△M.A.K. and S.N.R. contributed equally.

Notes

The authors declare no competing financial interest.

REFERENCES

(1) Kubista, M.; Sjöback, R.; Eriksson, S.; Albinsson, B. Experimental Correction for the Inner-Filter Effect in Fluorescence Spectra. *Analyst (Cambridge, U. K.)* **1994**, *119*, 417−419.

(2) MacDonald, B. C.; Lvin, S. J.; Patterson, H. Correction of Fluorescence Inner Filter Effects and the Partitioning of Pyrene to Dissolved Organic Carbon. *Anal. Chim. Acta* **1997**, *338*, 155−162.

(3) He, H.; Li, H.; Mohr, G.; Kovacs, B.; Werner, T.; Wolfbeis, O. S. Novel Type of Ion-Selective Fluorosensor Based on the Inner Filter Effect: An Optrode for Potassium. *Anal. Chem.* **1993**, *65*, 123−127.

(4) Shao, N.; Zhang, Y.; Cheung, S.; Yang, R.; Chan, W.; Mo, T.; Li, K.; Liu, F. Copper Ion-Selective Fluorescent Sensor Based on the Inner Filter Effect Using a Spiropyran Derivative. *Anal. Chem.* **2005**, *77*, 7294−7303.

(5) Cao, X.; Shen, F.; Zhang, M.; Guo, J.; Luo, Y.; Li, X.; Liu, H.; Sun, C.; Liu, J. Efficient Inner Filter Effect of Gold Nanoparticles on the Fluorescence of CdS Quantum Dots for Sensitive Detection of Melamine in Raw Milk. *Food Control* **2013**, *34*, 221−229.

(6) Tang, Y.; Liu, Y.; Cao, A. Strategy for Sensor Based on Fluorescence Emission Red Shift of Conjugated Polymers: Applications in pH Response and Enzyme Activity Detection. *Anal. Chem.* **2013**, *85*, 825−830.

(7) Fery-Forgues, S.; Lavabre, D. Are Fluorescence Quantum Yields So Tricky to Measure? A Demonstration Using Familiar Stationery Products. *J. Chem. Educ.* **1999**, *76*, 1260.

(8) Dodabalapur, A. Organic Light Emitting Diodes. *Solid State Commun.* **1997**, *102*, 259−267.

(9) Lee, J.; Sundar, V. C.; Heine, J. R.; Bawendi, M. G.; Jensen, K. F. Full Color Emission from II-VI Semiconductor Quantum Dot-Polymer Composites. *Adv. Mater.* **2000**, *12*, 1102−1105.

(10) Jang, E.; Jun, S.; Jang, H.; Lim, J.; Kim, B.; Kim, Y. White-Light-Emitting Diodes with Quantum Dot Color Converters for Display Backlights. *Adv. Mater.* **2010**, *22*, 3076−3080.

(11) Kwak, J.; Lim, J.; Park, M.; Lee, S.; Char, K.; Lee, C. High-Power Genuine Ultraviolet Light-Emitting Diodes Based On Colloidal Nanocrystal Quantum Dots. *Nano Lett.* **2015**, *15*, 3793−3799.

(12) Bronstein, N. D.; Yao, Y.; Xu, L.; O'Brien, E.; Powers, A. S.; Ferry, V. E.; Alivisatos, A. P.; Nuzzo, R. G. Quantum Dot Luminescent Concentrator Cavity Exhibiting 30-Fold Concentration. *ACS Photonics* **2015**, *2*, 1576−1583.

(13) Slooff, L. H.; Bende, E. E.; Burgers, A. R.; Budel, T.; Pravettoni, M.; Kenny, R. P.; Dunlop, E. D.; Büchtemann, A. A Luminescent Solar Concentrator with 7.1% Power Conversion Efficiency. *Phys. Status Solidi RRL* **2008**, *2*, 257−259.

(14) Chino, E.; Tajiri, K.; Kawakami, H.; Ohira, H.; Kamijo, K.; Kaneko, H.; Kato, S.; Ozawa, Y.; Kurumisawa, T.; Inoue, K.; Endo, K.; Moriya, K.; Aragaki, T.; Murai, K. 25.1: Invited Paper: Development of Wide-Color-Gamut Mobile Displays with Four-Primary-Color LCDs. *Dig. Tech. Pap. - Soc. Inf. Disp. Int. Symp.* **2006**, *37*, 1221−1224.

(15) Xie, R.-J.; Hirosaki, N.; Takeda, T. Wide Color Gamut Backlight for Liquid Crystal Displays Using Three-Band Phosphor-Converted White Light-Emitting Diodes. *Appl. Phys. Express* **2009**, *2*, 22401.

(16) Eaton, S. W.; Lai, M.; Gibson, N. A.; Wong, A. B.; Dou, L.; Ma, J.; Wang, L.-W.; Leone, S. R.; Yang, P. Lasing in Robust Cesium Lead Halide Perovskite Nanowires. *Proc. Natl. Acad. Sci. U. S. A.* **2016**, *113*, 1993−1998.

(17) Choi, C. L.; Koski, K. J.; Olson, A. C. K.; Alivisatos, A. P. Luminescent Nanocrystal Stress Gauge. *Proc. Natl. Acad. Sci. U. S. A.* **2010**, *107*, 21306−21310.

(18) Raja, S. N.; Olson, A. C. K.; Thorkelsson, K.; Luong, A. J.; Hsueh, L.; Chang, G.; Gludovatz, B.; Lin, L.; Xu, T.; Ritchie, R. O.; Alivisatos, A. P. Tetrapod Nanocrystals as Fluorescent Stress Probes of Electrospun Nanocomposites. *Nano Lett.* **2013**, *13*, 3915−3922.

(19) Trepat, X.; Wasserman, M. R.; Angelini, T. E.; Millet, E.; Weitz, D. A.; Butler, J. P.; Fredberg, J. J. Physical Forces during Collective Cell Migration. *Nat. Phys.* **2009**, *5*, 426−430.

(20) Kim, W.; Ferguson, V. L.; Borden, M.; Neu, C. P. Application of Elastography for the Noninvasive Assessment of Biomechanics in Engineered Biomaterials and Tissues. *Ann. Biomed. Eng.* **2016**, *44*, 705−724.

(21) Lim, H. C.; Schulkin, B.; Pulickal, M. J.; Liu, S.; Petrova, R.; Thomas, G.; Wagner, S.; Sidhu, K.; Federici, J. F. Flexible Membrane Pressure Sensor. *Sens. Actuators, A* **2005**, *119*, 332−335.

(22) Chen, O.; Zhao, J.; Chauhan, V. P.; Cui, J.; Wong, C.; Harris, D. K.; Wei, H.; Han, S.; Fukumura, D.; Jain, R. K.; Bawendi, M. G.; Hospital, M. G. Compact High-Quality CdSe − CdS Core − Shell Nanocrystals with Narrow Emission. *Nat. Mater.* **2013**, *12*, 1−29.

(23) Carbone, L.; Nobile, C.; De Giorgi, M.; Sala, F.; Della Morello, G.; Pompa, P.; Hytch, M.; Snoeck, E.; Fiore, A.; Franchini, I. R.; Nadasan, M.; Silvestre, A. F.; Chiodo, L.; Kudera, S.; Cingolani, R.; Krahne, R.; Manna, L. Synthesis and Micrometer-Scale Assembly of Colloidal CdSe/CdS Nanorods Prepared by a Seeded Growth Approach. *Nano Lett.* **2007**, *7*, 2942−2950.

(24) Raja, S. N.; Luong, A. J.; Zhang, W.; Lin, L.; Ritchie, R. O.; Alivisatos, A. P. Cavitation-Induced Stiffness Reductions in Quantum Dot−Polymer Nanocomposites. *Chem. Mater.* **2016**, *28*, 2540−2549.

(25) Hsu, C.-P.; Song, X.; Marcus, R. a. Time-Dependent Stokes Shift and Its Calculation from Solvent Dielectric Dispersion Data. *J. Phys. Chem. B* **1997**, *101*, 2546−2551.

(26) Talapin, D. V.; Nelson, J. H.; Shevchenko, E. V.; Aloni, S.; Sadtler, B.; Alivisatos, A. P. Seeded Growth of Highly Luminescent CdSe/CdS Nanoheterostructures with Rod and Tetrapod Morphologies. *Nano Lett.* **2007**, *7*, 2951−2959.

(27) Talapin, D. V.; Koeppe, R.; Götzinger, S.; Kornowski, A.; Lupton, J. M.; Rogach, A. L.; Benson, O.; Feldmann, J.; Weller, H. Highly Emissive Colloidal CdSe/CdS Heterostructures of Mixed Dimensionality. *Nano Lett.* **2003**, *3*, 1677−1681.

(28) Nirmal, M.; Murray, C. B.; Bawendi, M. G. Fluorescence-Line Narrowing in CdSe Quantum Dots: Surface Localization of the

Photogenerated Exciton. *Phys. Rev. B: Condens. Matter Mater. Phys.* **1994**, *50*, 2293−2300.

(29) van Sark, W. G. J. H. M.; Frederix, P. L. T. M.; Van den Heuvel, D. J.; Gerritsen, H. C.; Bol, A. a; van Lingen, J. N. J.; de Mello Donegá, C.; Meijerink, A. Photooxidation and Photobleaching of Single CdSe/ZnS Quantum Dots Probed by Room-Temperature Time-Resolved Spectroscopy. *J. Phys. Chem. B* **2001**, *105*, 8281−8284.

(30) Li, X.-Q.; Arakawa, Y. Optical Linewidths in an Individual Quantum Dot. *Phys. Rev. B: Condens. Matter Mater. Phys.* **1999**, *60*, 1915−1920.

(31) Whitham, P. J.; Knowles, K. E.; Reid, P. J.; Gamelin, D. R. Photoluminescence Blinking and Reversible Electron Trapping in Copper-Doped CdSe Nanocrystals. *Nano Lett.* **2015**, *15*, 4045−4051.

(32) Mork, A. J.; Weidman, M. C.; Prins, F.; Tisdale, W. A. Magnitude of the Förster Radius in Colloidal Quantum Dot Solids. *J. Phys. Chem. C* **2014**, *118*, 13920−13928.

(33) Raja, S. N.; Zherebetskyy, D.; Wu, S.; Ercius, P.; Powers, A.; Olson, A. C. K.; Du, D. X.; Lin, L.; Govindjee, S.; Wang, L.-W.; Xu, T.; Alivisatos, A. P.; Ritchie, R. O. Mechanisms of Local Stress Sensing in Multifunctional Polymer Films Using Fluorescent Tetrapod Nanocrystals. *Nano Lett.* **2016**, *16*, 5060−5067.

(34) Deirmendjian, D.; Clasen, R.; Viezee, W. Mie Scattering with Complex Index of Refraction. *J. Opt. Soc. Am.* **1961**, *51*, 620.

(35) Prazeres, T. J. V; Fedorov, A.; Barbosa, S. P.; Martinho, J. M. G.; Berberan-Santos, M. N. Accurate Determination of the Limiting Anisotropy of Rhodamine 101. Implications for Its Use as a Fluorescence Polarization Standard. *J. Phys. Chem. A* **2008**, *112*, 5034−5039.

(36) Qian, H.; Elson, E. L. Analysis of Confocal Laser-Microscope Optics for 3-D Fluorescence Correlation Spectroscopy. *Appl. Opt.* **1991**, *30*, 1185.

(37) Komaragiri, U.; Begley, M. R.; Simmonds, J. G. The Mechanical Response of Freestanding Circular Elastic Films Under Point and Pressure Loads. *J. Appl. Mech.* **2005**, *72*, 203.

(38) Nguyen, T. D.; Deshmukh, N.; Nagarah, J. M.; Kramer, T.; Purohit, P. K.; Berry, M. J.; McAlpine, M. C. Piezoelectric Nanoribbons for Monitoring Cellular Deformations. *Nat. Nanotechnol.* **2012**, *7*, 587−593.

(39) Takeda, M.; Ina, H.; Kobayashi, S. Fourier-Transform Method of Fringe-Pattern Analysis for Computer-Based Topography and Interferometry. *J. Opt. Soc. Am.* **1982**, *72*, 156.

(40) Bergert, M.; Erzberger, A.; Desai, R. A.; Aspalter, I. M.; Oates, A. C.; Charras, G.; Salbreux, G.; Paluch, E. K. Force Transmission during Adhesion-Independent Migration. *Nat. Cell Biol.* **2015**, *17*, 524−529.

(41) Charras, G.; Sahai, E. Physical Influences of the Extracellular Environment on Cell Migration. *Nat. Rev. Mol. Cell Biol.* **2014**, *15*, 813−824.

(42) Hanson, L.; Zhao, W.; Lou, H.-Y.; Lin, Z. C.; Lee, S. W.; Chowdary, P.; Cui, Y.; Cui, B. Vertical Nanopillars for *in Situ* Probing of Nuclear Mechanics in Adherent Cells. *Nat. Nanotechnol.* **2015**, *10*, 554−562.

(43) Singh, N.; Chen, J.; Koziol, K. K.; Hallam, K. R.; Janas, D.; Patil, A. J.; Strachan, A.; Hanley, J. G.; Rahatekar, S. S. Chitin and Carbon Nanotube Composites as Biocompatible Scaffolds for Neuron Growth. *Nanoscale* **2016**, *8*, 8288−8299.

(44) Butcher, D. T.; Alliston, T.; Weaver, V. M. A Tense Situation: Forcing Tumour Progression. *Nat. Rev. Cancer* **2009**, *9*, 108−122.

(45) Agha, R.; Ogawa, R.; Pietramaggiori, G.; Orgill, D. P. A Review of the Role of Mechanical Forces in Cutaneous Wound Healing. *J. Surg. Res.* **2011**, *171*, 700−708.

(46) Colin-York, H.; Shrestha, D.; Felce, J. H.; Waithe, D.; Moeendarbary, E.; Davis, S. J.; Eggeling, C.; Fritzsche, M. Super-Resolved Traction Force Microscopy (STFM). *Nano Lett.* **2016**, *16*, 2633−2638.

(47) Zaritsky, A.; Welf, E. S.; Tseng, Y.-Y.; Angeles Rabadán, M.; Serra-Picamal, X.; Trepat, X.; Danuser, G. Seeds of Locally Aligned Motion and Stress Coordinate a Collective Cell Migration. *Biophys. J.* **2015**, *109*, 2492−2500.

(48) Greytak, A. B.; Allen, P. M.; Liu, W.; Zhao, J.; Young, E. R.; Popović, Z.; Walker, B.; Nocera, D. G.; Bawendi, M. G. Alternating Layer Addition Approach to CdSe/CdS Core/shell Quantum Dots with near-Unity Quantum Yield and High on-Time Fractions. *Chem. Sci.* **2012**, *3*, 2028−2034.

(49) Jasieniak, J.; Smith, L.; Embden, J.; van Mulvaney, P.; Califano, M. Re-Examination of the Size-Dependent Absorption Properties of CdSe Quantum Dots. *J. Phys. Chem. C* **2009**, *113*, 19468−19474.

(50) Chen, O.; Zhao, J.; Chauhan, V. P.; Cui, J.; Wong, C.; Harris, D. K.; Wei, H.; Han, H.-S.; Fukumura, D.; Jain, R. K.; Bawendi, M. G. Compact High-Quality CdSe−CdS Core−shell Nanocrystals with Narrow Emission Linewidths and Suppressed Blinking. *Nat. Mater.* **2013**, *12*, 445−451.

(51) Raja, S. N.; Olson, A. C. K.; Limaye, A.; Thorkelsson, K.; Luong, A.; Lin, L.; Ritchie, R. O.; Xu, T.; Alivisatos, A. P. Influence of Three-Dimensional Nanoparticle Branching on the Young's Modulus of Nanocomposites: Effect of Interface Orientation. *Proc. Natl. Acad. Sci. U. S. A.* **2015**, *112*, 6533−6538.

(52) Eisfeld, A.; Briggs, J. S. The J- and H-Bands of Organic Dye Aggregates. *Chem. Phys.* **2006**, *324*, 376−384.

(53) Valerini, D.; Cretí, A.; Lomascolo, M.; Manna, L.; Cingolani, R.; Anni, M. Temperature Dependence of the Photoluminescence Properties of Colloidal CdSe/ZnS core/Shell Quantum Dots Embedded in a Polystyrene Matrix. *Phys. Rev. B: Condens. Matter Mater. Phys.* **2005**, *71*, 235409.